

Structural asymmetry induced high Curie temperature and large out-of-plane piezoelectricity in Gd_2COF MXenes and Gd_2COF/MoS_2 heterostructure

Yan Hu(胡焱), Yu-Ling Song(宋玉玲), Yu-Hong Huang(黄育红), Shu-Yao Cao(曹舒尧), and Fei Ma(马飞)
Citation: Chin. Phys. B, 2026, 35 (**7**): 077102. DOI: 10.1088/1674-1056/ae815f
http://cpb.iphy.ac.cn; http://iopscience.iop.org/cpb

What follows is a list of articles you may be interested in

Synthesis, structure and physical properties of ternary Ce-based compound Ce_3VAs_5

B S Min(闵保森), L C Fu(傅立承), X M Chen(陈晓铭), L C Shi(史鲁川), H Y Zheng(郑皓宇), J Zhang(张俊), J Song(宋静), Z Deng(邓正), J F Zhao(赵建发), L Duan(段磊), C J Xiao(肖长江), J L Zhu(朱金龙), X C Wang(望贤成), and C Q Jin(靳常青)
Chin. Phys. B, 2026, 35 (**5**): 057111. DOI: 10.1088/1674-1056/ae1ded

Charge-transfer-induced re-entrant ferromagnetism in twisted-bilayer-$MoTe_2$/hBN/WSe_2

Shaozheng Wang(王绍政), Xumin Chang(常旭敏), Feng Liu(刘峰), Yuchen Zheng(郑宇辰), Juncai Wu(吴俊才), Tong Zheng(郑桐), Kenji Watanabe, Takashi Taniguchi, and Shengwei Jiang(姜生伟)
Chin. Phys. B, 2026, 35 (**2**): 027101. DOI: 10.1088/1674-1056/ae1c27

Anionic electron dimensionality and monolayer ferromagnetism in Y-Co electrides

Lu Zheng(郑璐), Zimeng Lv(吕梓萌), Xiaochen Huang(黄小琛), Zhuangfei Zhang(张壮飞), Chao Fang(房超), Yuewen Zhang(张跃文), Qianqian Wang(王倩倩), Liangchao Chen(陈良超), Xiaopeng Jia(贾晓鹏), Biao Wan(万彪), and Huiyang Gou(缑慧阳)
Chin. Phys. B, 2025, 34 (**9**): 097105. DOI: 10.1088/1674-1056/adf82f

Simultaneous control of ferromagnetism and ferroelasticity by oxygen octahedral backbone stretching

Genhao Liang(梁根豪), Hui Cao(曹慧), Long Cheng(成龙), Junkun Zha(查君坤), Mingrui Bao(保明睿), Fei Ye(叶飞), Hua Zhou(周华), Aidi Zhao(赵爱迪), and Xiaofang Zhai(翟晓芳)
Chin. Phys. B, 2024, 33 (**9**): 097101. DOI: 10.1088/1674-1056/ad553c

High-temperature ferromagnetism and strong π-conjugation feature in two-dimensional manganese tetranitride

Ming Yan(闫明), Zhi-Yuan Xie(谢志远), and Miao Gao(高淼)
Chin. Phys. B, 2023, 32 (**3**): 037104. DOI: 10.1088/1674-1056/acae7b

---

Structural asymmetry induced high Curie temperature and large out-of-plane piezoelectricity in Gd_2COF MXenes and Gd_2COF/MoS_2 heterostructure

Yan Hu(胡焱)[1,2,†], Yu-Ling Song(宋玉玲)[3], Yu-Hong Huang(黄育红)[4], Shu-Yao Cao(曹舒尧)[5], and Fei Ma(马飞)[6,‡]

[1] *School of Electronic Information, Huzhou College, Huzhou* 313000, *China*
[2] *Huzhou Key Laboratory for Urban Multidimensional Perception and Intelligent Computing, Huzhou College, Huzhou* 313000, *China*
[3] *College of Physics and Electronic Engineering, Nanyang Normal University, Nanyang* 473061, *China*
[4] *School of Physics & Information Technology, Shaanxi Normal University, Xi'an* 710119, *China*
[5] *School of Physics and Electronic Information, Yan'an University, Yan'an* 716000, *China*
[6] *State Key Laboratory for Mechanical Behavior of Materials, Xi'an Jiaotong University, Xi'an* 710119, *China*

(Received 16 March 2026; revised manuscript received 23 June 2026; accepted manuscript online 24 June 2026)

Two-dimensional (2D) rare-earth (RE) ferromagnetic (FM) materials exhibit significant potential for next-generation spintronic devices. In this work, first-principles calculations are performed to study the MXene Gd_2COF monolayer. We demonstrate that Gd_2COF is a ferromagnetic half-metal with a large magnetic moment of 13 μ_B per formula unit and a Curie temperature (T_C) of 750 K, the highest one among the reported RE monolayers. The high T_C is attributed to both the out-of-plane structural asymmetry induced interlayer FM double-exchange interaction and the dual intralayer FM super-exchange pathways. Additionally, the system possesses a wide band gap of 3.09 eV and a magnetic anisotropy energy (MAE) of -0.25 meV, features consistent with half-metallicity and ferromagnetism. The monolayer Gd_2COF is metallic with $-5\% \sim -4\%$ biaxial strain, transforms into a half-metal with $-3\% \sim 3\%$ biaxial strain, and then becomes a semiconductor with $4\% \sim 5\%$ biaxial strain. It has a high Curie temperature of 550 K $\sim$ 900 K throughout the entire strain range. The Curie temperature decreases with increasing biaxial strain due to the weakened Gd–Gd and Gd–C/O/F bonds. Furthermore, the monolayer exhibits significant out-of-plane piezoelectricity at tensile strains of 4% and 5%. Furthermore, the planar Gd_2COF can be stabilized when supported on monolayer MoS_2 substrate to avoid bending. The Gd_2COF/MoS_2 heterostructure also has a high Curie temperature of 550 K $\sim$ 900 K with $-5\% \sim 5\%$ biaxial strain. The metal–half-metal–semiconductor transition and large piezoelectricity with strain can be similarly observed in this heterostructure.

Keywords: rare-earth metal, ferromagnetism, piezoelectricity

PACS: 71.20.Eh, 77.80.B–, 77.84.–s

DOI: 10.1088/1674-1056/ae815f **CSTR:** 32038.14.CPB.ae815f

1. Introduction

Two-dimensional (2D) ferromagnetic (FM) materials possess ultrathin structure and high surface-to-volume ratio, making them promising candidates for applications in high-speed and energy-efficient devices.[1,2] 2D FM materials exhibit numerous intriguing properties, such as the proximity effect,[3,4] anomalous quantum Hall effect,[5–7] multiferroicity,[8–10] skyrmion formation[11,12] and large tunnel magnetoresistance.[13] In fact, the non-magnetic 2D systems, for example, graphene could be induced into ferromagnetism by transition metal (TM) doping, hydrogen adsorption or introduction of vacancies. However, the resulting magnetism is generally weak.[14,15] Interestingly, CrI_3 monolayers[16] and bilayer $Cr_2Ge_2Te_6$[17] exhibit the intrinsic ferromagnetism at the monolayer limit. The results demonstrate that the long-range magnetic order can be stabilized in two dimensions through magnetic anisotropy arising from out-of-plane structural asymmetry. Subsequently, various intrinsic 2D FM monolayers and thin films, Fe_3GeTe_2[18] and 1T-VSe_2[19] monolayers, as well as MnS_2,[20] CrTe[21] and Cr_3Te_4[22] thin films, were studied recently. In particular, a series of 2D FM materials, such as MX_2 (M = Fe, Co, Ni; X = Cl, Br, I),[23] MX_3 (M = V–Ni; X = Cl, Br, I),[24–29] $CrGa_2Se_4$,[30] MnB,[31] metal-organic frameworks (MOFs),[32] MOX (M = Cr, Mn; X = Cl, Br),[33,34] FeB_3,[35] MnB_6,[36] and Co_2B_6[37] have been theoretically investigated. Nevertheless, the Curie temperatures of most 2D FM materials are still lower than room temperature,[18,23,24,27–30,33,34,36,38–48] posing a significant challenge for the development of 2D ferromagnets suitable for practical applications.

For TM ferromagnets, the crystal structure plays a crucial role in determining the Curie temperature. For instance, isovalent alloying can reduce the exchange gap of Cr ions in monolayer CrI_3[49] and CrOX (X = Cl, Br),[50] which enhances both the virtual hopping effect and the ferromagnetic coupling, and

†Corresponding author. E-mail: huyan@zjhzu.edu.cn
‡Corresponding author. E-mail: mafei@mail.xjtu.edu.cn

© 2026 Chinese Physical Society and IOP Publishing Ltd. All rights, including for text and data mining, AI training, and similar technologies, are reserved.

thus significantly elevates the Curie temperature from 45 K to 180 K, from 100 K to 310 K, and from 50 K to 320 K, respectively.[49,50] Additionally, lattice strain has been demonstrated to substantially enhance the Curie temperature of 2D TM ferromagnets.[34,49] Since the real hopping from double-exchange interaction is generally stronger than the virtual hopping from super-exchange mechanisms, designing 2D FM TM materials with magnetic ions in different spin states can induce real hopping and elevate the Curie temperature, such as in monolayer Cr_3X_4 (X = Se, Te)[51] and Fe_2X (X = S, Se).[52]

Rare-earth (RE) elements are promising for inducing substantial magnetic moments via f-electrons,[53] and have potential applications in higher-density spintronic devices. Moreover, heavier RE ions usually exhibit stronger magnetic anisotropy due to the enhanced spin–orbit coupling (SOC), which can stabilize the magnetic order against thermal fluctuations. 2D FM RE materials, such as Gd_2C,[54] EuN[55] and SmN[56] thin films, as well as $Ln = X_2$ (Ln = Eu, Gd; X = Si, Ge) monolayers,[57] have been synthesized, in which magnetism often arises from the delocalized d-electrons, and the ferromagnetism can be mediated by the f–d–p–d–f exchange mechanism with d-electrons as intermediaries. However, this mechanism is generally weaker than the d–p hybridization effect in many 2D TM ferromagnets, so that the Curie temperatures of most 2D FM RE monolayers are still low, in the range of 17 K $\sim$ 281 K.[58–66] It is still a challenge to design 2D RE ferromagnets with high Curie temperatures for potential applications in RE-based spintronics.

MXenes, a family of 2D materials with the general formula $M_{n+1}X_n$ (where M is a metal and X is C or N), can be selectively functionalized with O, F, and Cl,[67] in which the multiple M layers can introduce additional interlayer FM interactions. Furthermore, inequivalent magnetic sites can be created, enabling double-exchange interactions, by constructing double-metal layers or employing asymmetric surface functionalization. This makes MXenes ideal platforms for exploring high-Curie-temperature 2D ferromagnets. It has been predicted that the asymmetric MXenes, for example, Cr_2COF, Cr_2COCl, $Cr_2CO(OH)$[68] and CoMnC[69] monolayers possess high Curie temperatures of 622 K $\sim$ 1366 K. Moreover, similar to VSSe Janus monolayers,[70] the broken out-of-plane symmetry can induce built-in electric fields and out-of-plane piezoelectricity. Can we design asymmetric MXene-based RE monolayers with both high Curie temperature and out-of-plane piezoelectricity?

In this work, first-principles calculations are done to investigate the stability, electronic structure, and magnetic properties of RE-based Gd_2COF MXene monolayer. It is found that Gd_2COF is an FM half-metal with a high Curie temperature of 750 K and a sizable magnetic anisotropy energy (MAE) of -0.25 meV per formula unit, a large band gap of 3.09 eV. The high Curie temperature can be ascribed to the broken structural symmetry-induced interlayer FM interaction and the double-exchange mechanism, since other predicted FM RE monolayers are super-exchange ferromagnets.[58–66,71–79] This value is much higher than those of other FM RE monolayers (Table S1), in particular, higher than those of monolayers T-Gd_2C (322 K)[71] and Gd_2B_2 (550 K),[72] both of which exhibit interlayer super-exchange ferromagnetism. Under the biaxial strain of $-5\% \sim 5\%$, Gd_2COF undergoes phase transition from metal to half-metal and then semiconductor. Notably, the Curie temperature remains above room temperature (300 K) across the strain range, underscoring the robust ferromagnetism. Moreover, the asymmetric structure can induce large out-of-plane piezoelectricity. The planar Gd_2COF can be stabilized when supported on monolayer MoS_2 substrate to avoid bending.

2. Computational methods

All the calculations are performed by spin-polarized density function theory (DFT) as implemented in the Vienna *ab-initio* simulation package (VASP).[80] Interactions between electrons and nuclei are described by the projector augmented wave (PAW)[81,82] and the electronic exchange–correlation interactions are described by the Perdew–Burke–Ernzerhof (PBE) functional of the generalized gradient approximation (GGA).[83] Particularly, the Hubbard U terms are adopted to calculate the strong-correlated interaction, the coulomb interaction parameter U (9.2 eV) and the exchange interaction parameter J (1.2 eV) are used to describe the behaviors of Gd-f electrons,[60,61] particularly, the Heyd–Scuseria–Ernzerh (HSE06) method with the screening parameter fixed at a value of 0.2 $Å^{-1}$ was adopted to calculate the electronic band structure for comparison.[84]

The Brillouin zone integration is carried out by $9 \times 9 \times 1$ k-mesh based on the Monkhorst–Pack scheme.[85] The cut-off energy for the plane wave basis set is set as 500 eV. *Ab-initio* molecular dynamics (AIMD) simulations last for 5 ps with a time step of 2 fs in the NVT ensemble at 300 K by the Nose–Hoover method.[86] The harmonic and anharmonic phonon spectra are calculated using the Phonopy[87] and Dynaphopy codes[88] implemented within the VASP package, respectively. The convergence criterion for the total energy and force is set as 1×10^{-8} eV and 0.001 eV/Å, respectively. The crystal occupation Hamiltonian population (COHP) method employed in LOBSTER is applied to investigate the bonding and antibonding states.[89] The DFT-D3 method is employed to describe the weak dispersion forces of the van der Waals interactions for Gd_2COF/MoS_2 heterostructure.[90] A vacuum space of 20 Å is added along the direction perpendicular to the surface for both monolayer Gd_2COF and Gd_2COF/MoS_2

heterostructure to avoid interactions between the adjacent periodic units.

3. Results and discussion

3.1. Structural properties, ground state and stability of Gd_2COF monolayer

The pristine Gd_2C monolayer consists of a honeycomb lattice formed by top and bottom Gd triangular sub-layers, with C ions sandwiched between them in the space group of *P*-3*M*1 (Figs. 1(a) and 1(b)). Each Gd ion is coordinated to three nearest C ions, while each C ion is surrounded by six nearest Gd ions. On the pristine Gd_2C monolayer, there are two nonequivalent adsorption sites: site A, directly above a Gd ion, and site B, below a C ion, so there are four possible configurations for Gd_2COF monolayer (Figs. 1(c)–1(f)), for type-I (II) configuration, both F and O ions are located at A (B) site, while for type-III (IV) configuration, O ion is located at A (B) site but F ion is located at B (A) site. Type-I configuration is the most stable one (Table S2), suggesting a preferential hybridization between F/O and Gd ions due to the lower electronegativity of Gd ion. Based on a $2\times1\times1$ supercell, one ferromagnetic (FM), two antiferromagnetic (AFM-1 and AFM-2), and ferrimagnetic (FiM) states are examined (Fig. S1), for the FM state, all the Gd ions are coupled ferromagnetically (Fig. S1(a)), for the AFM-1 (AFM-2) state (Figs. S1(b) and S1(c)), the nearest-neighbor (NN) intralayer (interlayer) Gd ions are coupled ferromagnetically while the NN interlayer (intralayer) Gd ions are coupled anti-ferromagnetically, for the FiM state, one Gd_2 ions are coupled anti-ferromagnetically with other 3 Gd ions (Fig. S1(d)). The FM state is identified as the magnetic ground state. The optimized lattice parameters *a* and *b* are both 3.65 Å, which is close to the value of pristine Gd_2C (3.62 Å).[71] After functionalization, two inequivalent Gd sites, Gd_1 and Gd_2, emerge. The Gd_1–C and Gd_1–O bond lengths are 2.80 Å and 2.22 Å, respectively, while the Gd_2–C and Gd_2–F bond lengths are 2.47 Å and 2.42 Å, respectively. This leads to the broken out-of-plane symmetry in the Gd_2COF monolayer.

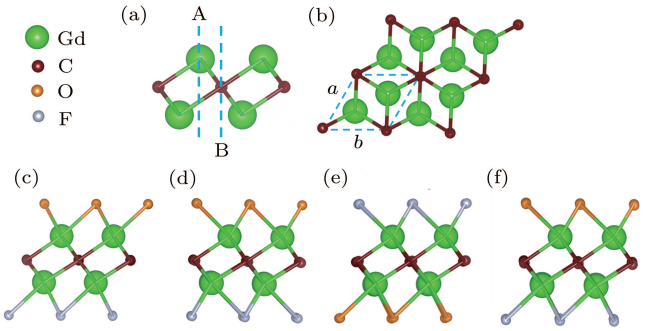


Fig. 1. (a) Side and (b) top views of the atomic structures of MXenes Gd_2C. A and B represent the two possible absorption sites for the termination F and O groups. (c)–(f) Four possible configurations of Gd_2COF. The areas circulated by dash lines represent the primitive cell.

The absorption energy is calculated using the following equation:

$$E_{\text{absorb}} = E_{Gd_2COF} - E_{Gd_2C} - E_F - E_O - \Delta_F - \Delta_O, \quad (1)$$

where E_{Gd_2COF} and E_{Gd_2C} are the total energies of Gd_2COF and Gd_2C monolayers, E_O and E_F are the atomic energies of O_2 and F_2 gas, $\Delta\mu = \mu - (1/2)E(T_2)$, μ is the chemical potential of O and F atoms. At the temperature range of 0 K∼300 K, $\Delta\mu$ of both O and F atoms is in the range of 0 eV ∼ −0.32 eV.[91] Accordingly, the absorption energies are in the range of −10.86 eV ∼ −10.22 eV per formula unit for the Gd_2COF monolayer. The negative values confirm that the formation process remains exothermic, there are no imaginary frequencies across the Brillouin zone in the phonon spectra of Gd_2COF monolayer at 0 K and 300 K, indicating dynamic stability (Figs. 2(a) and 2(b)). Moreover, AIMD simulations revealed that no bond breaking and reconstruction occur in the Gd_2COF monolayer at 300 K (Fig. 2(c)), thermal oscillation of the whole structure happens near the equilibrium position, indicating good thermal stability, therefore we believe that Gd_2COF monolayer can be synthesized and its structure can remain stable at room temperature.

Finally, the independent elastic constants C_{11} and C_{12} are calculated to be 123.67 N/m and 55.48 N/m for Gd_2COF monolayer, respectively. According to the isotropic lattice symmetry, the elastic constant C_{22} is equal to C_{11}, and $C_{66} = \frac{1}{2}(C_{11} - C_{12})$, thus C_{22} and C_{66} are 123.67 N/m and 34.10 N/m respectively. These elastic constants satisfy the Born–Huang stability criteria: $C_{11} > 0$, $C_{11}C_{22} - C_{12}^2 > 0$ and $C_{66} > 0$,[92] confirming that the Gd_2COF monolayer is mechanically stable. Figure 2(d) shows the calculated Young's modulus of Gd_2COF monolayer; it is isotropic with a value of 98.78 N/m, which is much larger than that of CrI_3 monolayer (23.85 N/m).[93]

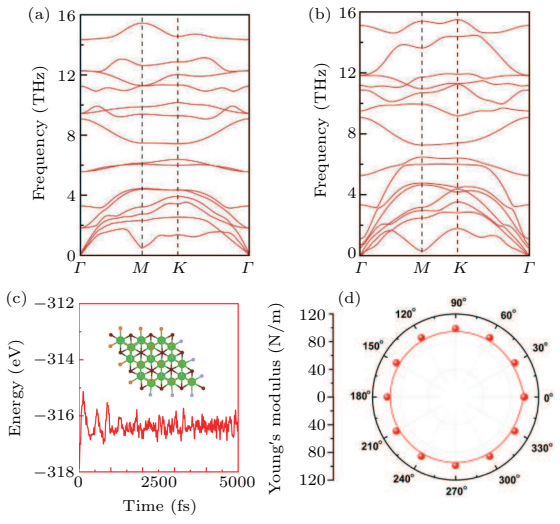


Fig. 2. Phonon spectra at (a) 0 K and (b) 300 K. (c) MD simulated energy evolution and snapshots of atomic configurations at the end of 5 ps AIMD simulation at 300 K, (d) angular dependence of the Young's modulus for Gd_2COF monolayer.

3.2. Electronic and magnetic properties of Gd_2COF monolayer

Figure 3(a) shows the spin-resolved band structures. The Gd_2COF monolayer is a half-metal with an indirect band gap of 3.09 eV. It possesses a metallic spin-up channel and a semiconducting spin-down channel, with the valence band maximum (VBM) and the conduction band minimum (CBM) at −0.46 eV and 2.63 eV, respectively. According to the Fermi–Dirac distribution,[94] the thermally induced occupation probability between the valence band and the Fermi level at 300 K is on the order of 10^8, ensuring the stability of the half-metallic feature. As shown in Fig. 3(b), the f orbitals of both Gd_1 and Gd_2 ions are highly localized and far from the Fermi level. Therefore, the d–p hybridization between Gd and C/O/F ions plays a crucial role in inducing ferromagnetism. Under the C_{3V} symmetry, the Gd-d orbitals split into d_{z^2}, e_1 ($d_{xz}+d_{yz}$), and e_2 ($d_{xy}+d_{x^2+y^2}$) groups. The VBM is dominated by the C-p_x/p_y orbitals while the CBM is dominated by the Gd_1-e_1 orbitals (Fig. S2(a)). Moreover, the hybridizations between Gd_1/Gd_2 and C ions are stronger than those between Gd_1–O/Gd_2–F ions. The spin-up and spin-down channels of O and F-p orbitals are almost fully occupied (Fig. S2(b)), corresponding to the valence electron configurations of $2s^2p^6$ for O and F ions, while the spin-up channel of C-p orbitals is partially occupied. Moreover, at the HSE06 level, the Gd_2COF monolayer is also a FM half-metal (Fig. S2(c)). According to the Bader analysis (Table S3), Gd_1 and Gd_2 ions donate 1.62 and 1.72 electrons to C ions, respectively, while O and F ions acquire 1.87 and 0.92 electrons from them, respectively. This results in a magnetic moment of 6/7 μ_B for Gd_1/Gd_2 ions but a negligible one on C, O, and F ions. The AFM-1 state converted to the FiM-1 state as well. To explain the origin of the electron transfer mechanism, we calculated the electron localization function (ELF) (Fig. S3). The values of ELF for the regions between Gd and C/O/F ions range from 0 to 0.25, reflecting the nature of Gd–C/O/F ionic bonding. Therefore, Gd ions can donate more electrons to C/O/F ions. In addition, more charge accumulates between the Gd and C ions, indicating that both Gd_1–C and Gd_2–C bonds have more covalent character than Gd_1–O and Gd_2—F bonds.

The magnetic ground state of Gd_2COF is governed by the interplay between the direct and indirect exchange interactions among Gd ions. The direct exchange interaction, mediated primarily by the nearly half-filled Gd-f orbitals, exhibits FM coupling between neighboring Gd ions, consistent with Hund's rule.[95] Simultaneously, the indirect exchange interaction arises from d–p hybridization between Gd ions and the surrounding C, O and F ions. According to the Goodenough–Kanamori–Anderson (GKA) rule,[96] when the bond angle between two Gd ions via a nonmagnetic ligand is close to 90°, the Gd-d orbitals tend to hybridize with orthogonal p orbitals of the C, O and F ions, leading to FM coupling between Gd ions according to the symmetry (Fig. S4(a)). As illustrated in Fig. 3(c), the calculated θ_1, θ_2, θ_3 and θ_4 are 91.3°, 81.2°, 110.6° and 98.0°, respectively, suggesting the existence of FM indirect exchange between both nearest-neighbor intralayer and interlayer Gd ions.

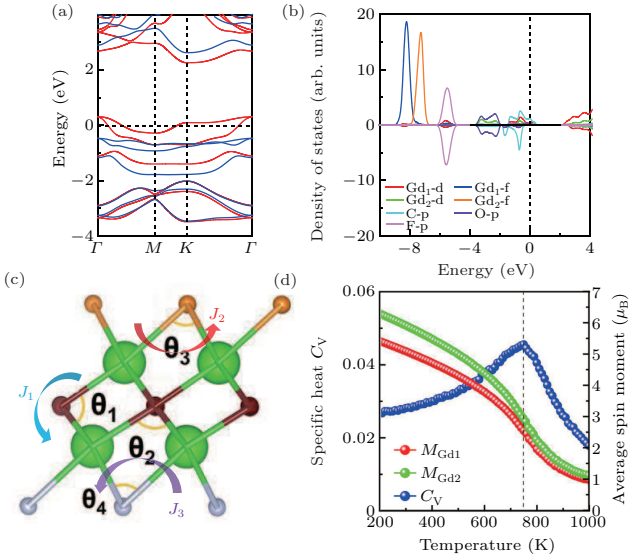


Fig. 3. (a) Spin-resolved electronic band structure, (b) projected density of states (PDOS) of Gd-d, Gd-f, C-p, F-p and O-p orbitals, (c) the illustrations of exchange coupling parameters J_1, J_2, J_3 and θ_1, θ_2, θ_3, θ_4, (d) the simulated averaged net magnetic moment of each Gd_1 and Gd_2 ion and specific heat with respect to temperature for Gd_2COF monolayer.

The magneto-crystalline anisotropy energy (MCE) is defined as the differences between the in-plane and out-of-plane magnetization directions, as $E_{MCE} = E_z - E_{x/y}$, where E_z and $E_{x(y)}$ denote the total energies when magnetization is aligned along z and x (y) axes, respectively. For Gd_2COF monolayer, the calculated MCE is −1.37 meV per formula unit, the negative value indicates that the easy magnetization axis is out-of-plane oriented. Given the large magnetic moment of Gd ions, we further calculated the magnetic dipolar energy (MDE) for Gd_2COF monolayer. For a FM system, the MDE in atomic Rydberg units is given by[97]

$$E_d = \sum_{ij} \frac{m_i m_j}{2c^2} M_{ij}, \tag{2}$$

where the speed of light $c = 137.036$ a.u., i/j are the atomic position vectors in the unit cell, and m_i/m_j is the atomic magnetic moment on sites i/j (in units of μ_B). The magnetic dipolar Madelung constant M_{ij} is calculated as

$$M_{ij} = \sum_R \frac{1}{|R+i+j|^3} \left\{ 1 - -3 \frac{[(R+i+j)\cdot \hat{m}_i]^2}{|R+i+j|^2} \right\}, \tag{3}$$

where R are the lattice vectors. The shape anisotropy energy ΔE_d (SAE) is calculated to be 0.474 meV and 0.646 meV for Gd_1 and Gd_2 ions, respectively, yielding a total SAE of

1.12 meV per formula unit of Gd_2COF, because the magnetostatic dipole–dipole interactions weaken the out-of-plane magnetic anisotropy. The net magnetic anisotropy energy (MAE) of Gd_2COF monolayer is -0.25 meV per formula unit, although this value is considerably smaller than the MCE, it remains notably larger than the MAE of bulk Fe (0.001 meV/atom)[98] and Ni (0.003 meV/atom),[98] such the MAE is sufficient to stabilize the long-range magnetic order in the Gd_2COF monolayer.

The magnetic exchange interactions between nearest-neighbor (NN) interlayer and intralayer Gd ions are described by the parameters J_1, J_2 and J_3 (Fig. 3(c)). The spin Hamiltonian is expressed as[99]

$$H = -\sum_{i,j} J_1 M_i M_j - \sum_{k,l} J_2 M_k M_l - \sum_{m,n} J_3 M_m M_n - A(M_i^z)^2, \quad (4)$$

where J_1, J_2 and J_3 are the exchange coupling parameters, M is the net magnetic moment of Gd ions, i and j (k and l, m and n) stand for the interlayer (intralayer) nearest neighboring Gd ions, A is the magnetic anisotropy parameter, M_i^z represents net magnetic moment per formula unit along a preferred axis and $A(M_i^z)^2$ is the total MCE. Correspondingly, the total energies of FM, AFM, FiM-1 and FiM-2 states in the $2\times1\times1$ supercell can be expressed as

$$E_{\mathrm{FM}} = E_0 - 6J_1 M_{\mathrm{Gd1}} M_{\mathrm{Gd2}} - 6J_2 M_{\mathrm{Gd1}}^2 - 6J_3 M_{\mathrm{Gd2}}^2, \quad (5)$$

$$E_{\mathrm{AFM}} = E_0 - 2J_1 M_{\mathrm{Gd1}} M_{\mathrm{Gd2}} + 2J_2 M_{\mathrm{Gd1}}^2 + 2J_3 M_{\mathrm{Gd2}}^2, \quad (6)$$

$$E_{\mathrm{FiM\text{-}1}} = E_0 + 6J_1 M_{\mathrm{Gd1}} M_{\mathrm{Gd2}} - 6J_2 M_{\mathrm{Gd1}}^2 - 6J_3 M_{\mathrm{Gd2}}^2, \quad (7)$$

$$E_{\mathrm{FiM\text{-}2}} = E_0 - 6J_2 M_{\mathrm{Gd1}}^2 + 2J_3 M_{\mathrm{Gd2}}^2. \quad (8)$$

The magnetic coupling parameters are derived from energy differences between FM and the other states:

$$J_1 = \frac{E_{\mathrm{FiM_1}} - E_{\mathrm{FM}}}{12 M_{\mathrm{Gd1}} M_{\mathrm{Gd2}}}, \quad (9)$$

$$J_3 = \frac{E_{\mathrm{FiM_2}} - E_{\mathrm{FM}} - 6J_1 M_{\mathrm{Gd1}} M_{\mathrm{Gd2}}}{8 M_{\mathrm{Gd2}}^2}, \quad (10)$$

$$J_2 = \frac{1}{M_{\mathrm{Gd1}}^2}\left[\frac{E_{\mathrm{AFM}} - E_{\mathrm{FM}} - 4J_1 M_{\mathrm{Gd1}} M_{\mathrm{Gd2}}}{8} - J_3 M_{\mathrm{Gd}}^2\right]. \quad (11)$$

The calculated J_1, J_2 and J_3 are 0.86 meV, 1.04 meV and 0.43 meV, respectively. The positive values indicate a preference for FM coupling. The Curie temperature (T_C) of the Gd_2COF monolayer is evaluated using statistical Monte Carlo (MC) simulations based on the Heisenberg model. A $100\times100\times1$ supercell containing 20000 magnetic moment vectors is employed, which lasts for 10^5 MC steps at each temperature. Magnetic moments are randomly rotated at each step. We estimated the T_C value of 42 K for CrI_3 monolayer,[98] in good agreement with the experimental value.[16] The results confirm the accuracy of the calculation method. As shown in Fig. 3(d), the specific heat C_V is defined as $C_V = (\langle E^2\rangle - \langle E\rangle^2)/(k_B T^2)$. The peak value of C_V corresponds to T_C of 750 K for Gd_2COF monolayer, which is higher than the T_C of other predicted 2D FM RE monolayers,[58–66,71–79] which range from 17 K to 648 K (Table S1). Apparently, the Gd_2COF monolayer possesses the highest T_C among all the predicted FM RE monolayers. Owing to the distinct spin states of Gd_1 and Gd_2 ions, the indirect interlayer coupling between the nearest-neighbor Gd ions is attributed to the double-exchange mechanism. As illustrated in Fig. S4(b), in this case ferromagnetism originates from interactions between the highest occupied Gd_2-d orbital and the lowest unoccupied Gd_1-d orbital based on the Pauli exclusion principle. The distinct spin states of Gd_1 and Gd_2 ions typically exhibit a smaller exchange d–d gap; thus the double-exchange mechanism driven by real electron hopping is beneficial to both FM coupling and high Curie temperature. In contrast, the indirect intralayer interactions between neighboring Gd_1 (or Gd_2) ions are governed by the super-exchange interaction, while in this case interactions between the highest occupied Gd_1-d (Gd_2-d) orbital and the lowest unoccupied Gd_1-d (Gd_2-d) orbital induce ferromagnetism (Fig. S4(c)). The virtual electron hopping brings a larger exchange d–d gap, which is unfavorable for FM coupling. But in addition to the Gd_1–C–Gd_1 (and Gd_2–C–Gd_2) pathways, super-exchange interaction between intralayer Gd_1 (or Gd_2) ions can also be mediated through Gd_1–O–Gd_1 (and Gd_2–F–Gd_2) routes. The multiple super-exchange pathways further enhance the overall FM coupling. The double-exchange interlayer coupling and the multi-path super-exchange intralayer interactions lead to robust FM ordering among Gd ions and high Curie temperature. At 750 K, monolayer Gd_2COF can also maintain dynamic and thermal stability (Fig. S5).

3.3. The effect of biaxial strain on Gd_2COF monolayer

Commonly, the Gd_2COF monolayer tends to bend along the out-of-plane direction. In a $3\times2\times1$ supercell model with a bending radius of 3.72 Å (Fig. 4(b)), the curved nanotube configuration exhibits the lowest energy, being more stable than the planar Gd_2COF monolayer by 0.008 eV/Å^2 (Figs. 4(c) and 4(d)). However, the planar Gd_2COF can be stabilized when supported on a monolayer MoS_2 substrate (Fig. S6), since the interfacial binding energy exceeds -0.008 eV/Å^2 (-0.024 eV/Å^2); the flat surface electrostatic potential in the regions on both sides of the heterojunction shows that the vacuum space is thick enough (Fig. S7). Moreover, the substrate can also induce biaxial strain which can modulate the electronic and magnetic properties[72] effectively. In this work, we systematically investigated the electronic and magnetic properties of the Gd_2COF monolayer under biaxial strain of $-5\%\sim+5\%$. It is found that the Gd_2COF monolayer maintains an FM ground state. The magnetic moments of Gd_1 and Gd_2 ions remain 6 μ_B and 7 μ_B, respec-

tively, but those of C, O, and F ions remain negligible. Consequently, the double-exchange interlayer coupling and the multi-path super-exchange intralayer interactions remain unchanged. Gd_2COF monolayer undergoes a phase transition from metal to half-metal and then to semiconductor (Fig. 5).

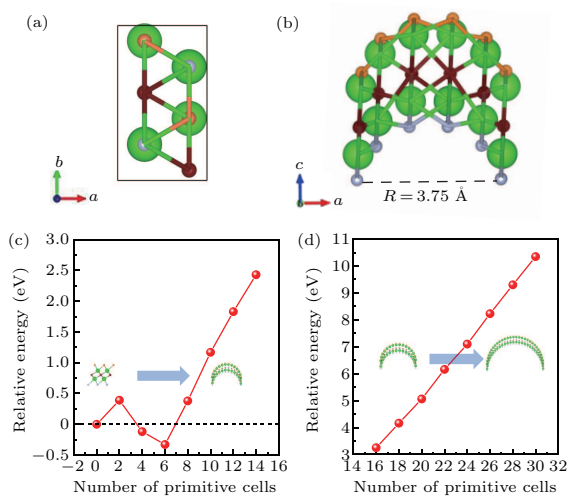


Fig. 4. (a) The primitive cell of a square lattice, (b) the curved nanotube in a square lattice with a $3\times2\times1$ supercell, the bending radius is 3.72 Å, (c)–(d) variation of the relative energy between the curved nanotube and the monolayer structure with the supercell size, the supercell can only extend in the x-direction.

Under the compressive strain of $-5\% \sim -4\%$, the electronic states from both spin-up and spin-down channels cross the Fermi level, characteristic of a FM metal. Under the strains of -3% and $+3\%$, the monolayer exhibits a robust half-metallic state: the spin-down channel has a band gap of about 3.05 eV, while the spin-up channel remains metallic. Under the strains below $+1\%$, the VBM increases firstly, and then decreases slightly, but the CBM changes in an opposite trend, the maximum VBM and CBM are 0.50 eV and 2.94 eV at the strains of $+1\%$ and -3%, respectively. At the larger tensile strains of $4\% \sim 5\%$, Gd_2COF monolayer transforms into a FM semiconductor, with both spin channels possess band gaps, in which the VBM and CBM are dominated by the spin-up channel with a band gap of 1.95 eV. At a strain of 4%, the VBM is only 0.15 eV below the Fermi level, leading to a thermally induced valence–Fermi level occupation probability on the magnitude order of 10^{-3} at 300 K (Fig. 6(a)).

With increasing strain, band structures move downwards overall because of weaker Coulomb repulsion, leading to phase transition from metal to half-metal and then to semiconductor. For both spin channels, occupied C-p_x/p_y orbitals have less weight in the highest occupied energy band, while unoccupied Gd_1-e_1 and e_2 orbitals have more weight in the lowest unoccupied energy band, indicating these orbitals are also more sensitive to the in-plane biaxial strain and thus tend to move downwards with increasing strain correspondingly (Fig. S8). On the other hand, under compressive strain, interactions between Gd-d and C-p orbitals become stronger, which makes both Gd-d and C-p orbitals more delocalized (Fig. S9). In the spin-up channel, a more delocalized highest occupied energy band crosses the Fermi level, resulting in half-metallicity. In contrast, under tensile strain, weaker interactions between Gd-d and C-p orbitals make these orbitals become more localized (Fig. S9); thus, in the spin-up channel, they become far from the Fermi level, and at -4% and -5% strain, both spin channels are semiconducting. Compared with Gd_2-d orbitals, hybridizations between Gd_1-d and C-p orbitals are more sensitive to the biaxial strain.

Considering the effect of substrate, under biaxial strain of $-5\% \sim -2\%$, the heterostructure is an FM metal, while it converts to a half-metal under biaxial strain of $-1\% \sim 3\%$. With biaxial strains of $4\% \sim 5\%$, it is still an FM semiconductor, and the magnetic moments of Gd_1 and Gd_2 ions remain unchanged throughout this strain range (Fig. S10).

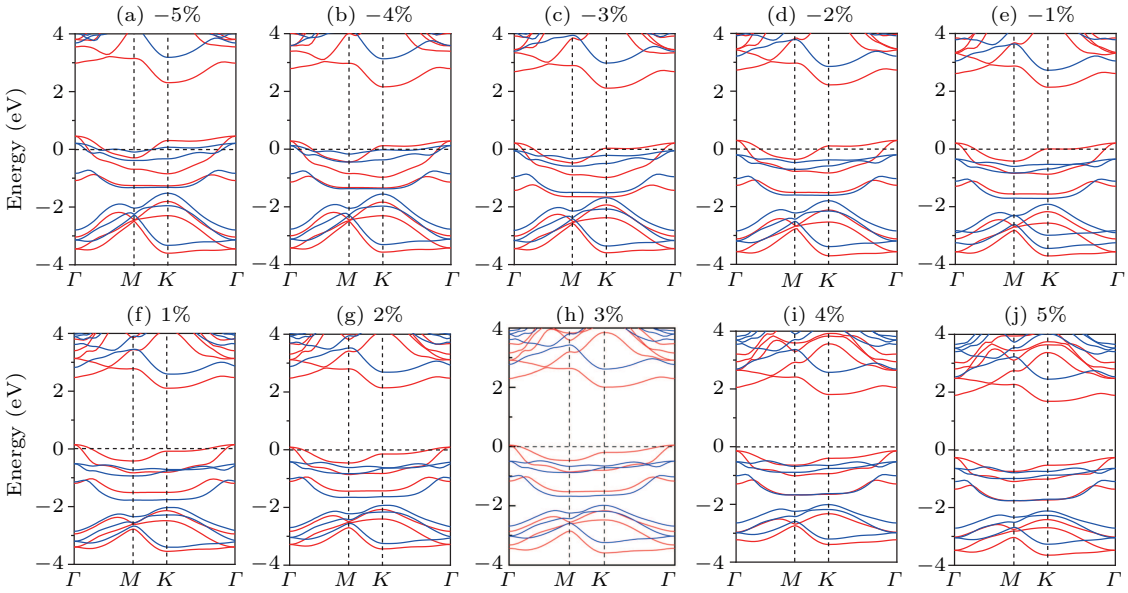


Fig. 5. Spin-resolved band structure for Gd_2COF monolayer under biaxial strain from -5% to 5%.

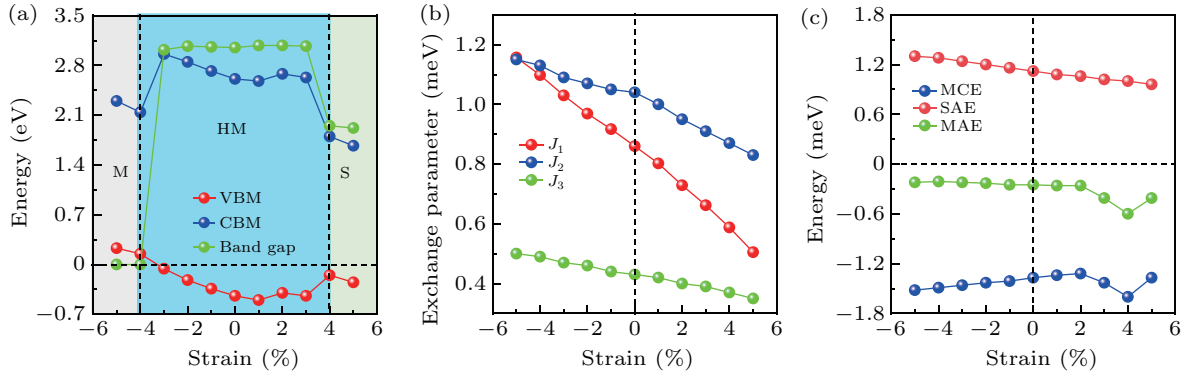


Fig. 6. (a) Valence band maximum (VBM), conduction band minimum (CBM), and band gap, M, HM and S represent metal, half-metal and semiconductor, respectively. (b) Exchange coupling parameters J_1, J_2 and J_3, (c) magneto-crystalline anisotropy energy (MCE), shape anisotropy energy (SAE) and magnetic anisotropy energy (MAE) per formula unit for Gd_2COF monolayer under biaxial strain from −5% to 5%.

Moreover, the structural asymmetry along the z-axis gives rise to out-of-plane piezoelectricity with the piezoelectric coefficient e_{31} of 56.3 pC/m and 78.2 pC/m in the Gd_2COF monolayer under a biaxial strain of 4% and 5%, respectively. This value is much larger than those of monolayers Janus MXY (M = Mo, W; X/Y = S, Se, Te) (1 ∼ 3.8 pC/m),[100] comparable to those of monolayer Y_2CO_2 (88 pC/m),[101] In_2Se_3 (51.7 pC/m),[102] yet smaller than those of Sc_2CO_2 (196 pC/m) and La_2CO_2 (120 pC/m),[101] in comparison with other FM monolayers, this value is much larger than those of CrSI (2 pC/m),[103] VSeTe (11 pC/m),[104] and VSTe (36 pC/m),[104] comparable to that of CrSBr (71 pC/m),[103] smaller than that of CrSCl (121 pC/m).[103] Since there have been no reports so far on the piezoelectricity of 2D FM RE materials, monolayer Gd_2COF would be a research hotspot in the field of RE piezoelectric ferromagnetism.

Consistent with M_2CO_2 (M = Sc, Y, La) monolayers,[101] the in-plane piezoelectric coefficients e_{11} of Gd_2COF, 287.3 pC/m and 354.2 pC/m at strains of 4% and 5%, are significantly larger than its out-of-plane coefficients. Moreover, both e_{11} and e_{31} for Gd_2COF/MoS_2 heterostructure at 4%/5% strain are 328.6/376.3 pC/m and 68.2/83.8 pC/m, respectively, indicating the piezoelectricity of Gd_2COF monolayer can be reinforced by the MoS_2 substrate.

Under the biaxial strains of −5% ∼ 5%, the magnetic exchange parameters J_1, J_2, and J_3 all decrease monotonically with increasing strain (Fig. 6(b)). Firstly, the direct FM exchange between Gd ions is weakened, because the Gd–Gd bond length is elongated under tensile strain. Secondly, quantitative descriptions of bonding characteristics by the COHP analyses are given in Fig. S11. The positive/negative values of –COHP denote the bonding/anti-bonding states; thus, both the Gd–C and Gd–O/F bonds are weakened under the tensile strain, which reduces the indirect FM exchange interactions and lowers the Curie temperature. The values of integrated orbital-projected –COHP (–IpCOHP) for both Gd_1–O (0.058) and Gd_2–F (0.017) bonds are close to zero (Fig. S11), indicating their stronger ionic bonding characteristic, which originates from the great differences in electronegativity between Gd (1.2) and O (3.44)/F (3.98) elements, while the larger values of –IpCOHP for both Gd_1–C and Gd_2–C bonds indicate these bonds have a more covalent tendency, which is in agreement with our previous analysis of the ELF. Moreover, compared with Gd_1–C bond, the smaller value of –COHP for Gd_2–C bond is probably due to its stronger ionic bonding feature, even though the Gd_2–C bond length is shorter. Throughout this strain range, the values of –IpCOHP for all specified interactions are still small, indicating all these bonds are still ionic.

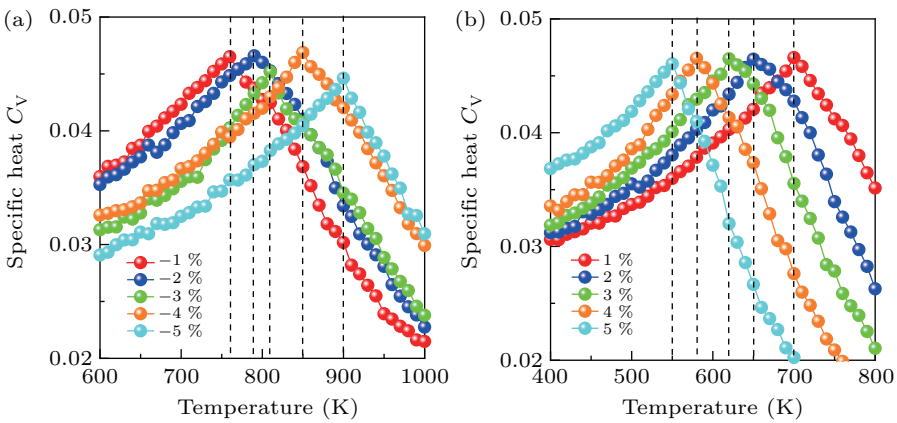


Fig. 7. (a) and (b) The simulated averaged specific heat with respect to temperature for Gd_2COF monolayer under biaxial strain from −5% to 5%.

Across the strain range of $-4\% \sim 5\%$, J_2 remains the largest one among the three parameters, attributable to the stronger super-exchange interactions along both Gd_1–C–Gd_1 and Gd_1–O–Gd_1 pathways. Although the interlayer nearest-neighbor Gd ions are mediated only by the Gd_1–C–Gd_2 exchange path, J_1 remains greater than J_3 due to the dominant role of the double-exchange mechanism. At a strain of -5%, J_1 and J_2 are nearly equal, the Curie temperature of the Gd_2COF monolayer decreases with increasing biaxial strain, from 900 K at -5% to 550 K at 5%, but remains above room temperature across the entire strain range (Figs. 7(a) and 7(b)). After considering the substrate effect, the J_1, J_2, and J_3 remain nearly unchanged throughout this strain range, positive values for J_1, J_2, and J_3 indicate a preference for FM coupling for both interlayer and intralayer NN Gd ions, the simulated Curie temperature for the Gd_2COF/MoS_2 heterostructure also remains unchanged (Fig. S12), except at $-1\%/4\%$ strain which the Curie temperature increased/decreased slightly to 760 K/580 K, respectively.

Throughout this strain range, the easy magnetization axis remains perpendicular to the *xy*-plane. The MCE reaches a maximum value of 1.62 meV at a strain of 4% (Fig. 6(c)). It decreases from 1.53 meV to 1.31 meV as the strain is changed from -5% to 2%, then increases at a strain of 4%, but decreases to 1.37 meV at a strain of 5%. In contrast, the SAE consistently favors in-plane magnetization. The magnitude of SAE decreases with increasing strain due to the enlarged *R*. Since the SAE contribution opposes that of MCE, the inclusion of SAE weakens the overall out-of-plane magnetic anisotropy. Nevertheless, the net MAE maintains the same easy axis direction as the MCE, with values ranging from 0.22 meV to 0.61 meV across the applied strain range.

4. Conclusion

In summary, we designed an asymmetric MXene monolayer Gd_2COF to modulate both interlayer FM and double-exchange interactions, for which the stability, electronic structure, and magnetic properties of Gd_2COF monolayer have been systematically investigated. Our findings demonstrate that Gd_2COF is an FM half-metal with a Curie temperature of 750 K, a spin-down band gap of 3.09 eV, and a significant out-of-plane MAE of -0.25 meV per formula unit, possessing the highest Curie temperature among the predicted 2D FM RE monolayers. The total magnetic moment is 13 μ_B per formula unit, predominantly contributed by the Gd ions. Under a biaxial strain of $-5\% \sim 5\%$, the system undergoes a phase transition from metal to half-metal and then to semiconductor. The Curie temperature decreases from 900 K to 550 K, as the biaxial strain is increased. This can be ascribed to the weakened direct and indirect FM exchange interactions, as a result of the elongated Gd–Gd bonds and the softened Gd–C/O/F bonds, respectively. The easy magnetization axis remains out-of-plane across the entire strain range. Furthermore, notable out-of-plane piezoelectricity is observed under tensile biaxial strains of 4% and 5%. More importantly, the planar Gd_2COF can be stabilized when supported on monolayer MoS_2 substrate to avoid bending, and the Gd_2COF/MoS_2 heterostructure also has a high Curie temperature of 550 K $\sim$ 900 K with $-5\% \sim 5\%$ biaxial strain. The metal–half-metal–semiconductor transition and large piezoelectricity with strain can be similarly observed in this heterostructure.

Acknowledgments

Project supported by the Initial Scientific Research Fund of Talent Introduction in Huzhou College (Grant No. RK64003), Huzhou National Science Fund Project (Grant No. 2025YZ49), the Zhejiang Provincial Natural Science Foundation of China (Grant No. ZCLQN26A0403), and the National Natural Science Foundation of China (Grant No. 12404040). This study was carried out at the Bingshui Riverside super-computing Center (Grant No. BRSC), and the calculations were performed on TianHe-2.

References

[1] Burch K S, Mandrus D and Park J G 2018 *Nature* **563** 47
[2] Zhang K, Han S, Lee Y, *et al.* 2021 *Adv. Mater.* **33** 2170029
[3] Gong C and Zhang X 2019 *Science* **363** 6428
[4] Zhang L M, Song L Y, Dai H W, *et al.* 2020 *Appl. Phys. Lett.* **116** 042402
[5] Zhang P, Si K P, Wang X G, Zhao F F, Li B X, Wei J T, Yang Y H, Tang P Z, Liu Z, Wu K and Gong Y J 2025 *Adv. Mater.* **37** e09261
[6] Li Y F, Zhang K, Pan Y, Wu D X, Lv H F, Wu X J and Yang J L 2025 *J. Phys. Chem. Lett.* **16** 5188
[7] He K, Ma X C, Chen X, Lv L, Wang Y Y and Xue Q K 2013 *Chin. Phys. B* **22** 067305
[8] Chen B J, Lin J H, Feng B, Ikuhara Y, Ohta H and Katayama T 2024 *Cryst. Growth Des.* **24** 8439
[9] Bai J B, Yang T, Guo Z Z, Liu Y, Jiao Y L, Meng W Z and Cheng Z X 2025 *Mater. Horiz.* **12** 2248
[10] Jiang X X, Wang Z K, Li C, Sun X L, Yang L, Li D M, Cui B and Liu D S 2024 *Chin. Phys. Lett.* **41** 057501
[11] Mi S, Guo J F, Hu G J, Wang G C, Li S Y, Gong Z Z, Jin S Z, Xu R, Peng F, Ji W, Yu W Q, Wang X L, Wang X Y, Yang H T and Cheng Z H 2024 *Nano Lett.* **24** 13094
[12] Du W H, Dou K Y, He Z L, Dai Y, Huang B B and Ma Y D 2022 *Nano Lett.* **22** 3440
[13] Zhu W K, Xie S H, Lin H L, *et al.* 2022 *Chin. Phys. Lett.* **39** 128501
[14] Krasheninnikov A V, Lehtinen P O, Foster A S, PyykkÖ P and Nieminen R M 2009 *Phys. Rev. Lett.* **102** 126807
[15] Zhou J, Wang Q, Sun Q, Chen X S, Kawazoe Y and Jena P 2009 *Nano Lett.* **9** 3867
[16] Huang B, Clark G, Moratalla E N, Klein D R, Cheng R, Seyler K L, Zhong D, Schmidgall E, McGuire M A, Cobden D H, Yao W, Xiao D, Herrero P J and Xu X 2017 *Nature* **546** 270
[17] Gong C, Li L, Li Z L, Ji H W, Stern A, Xia Y, Cao T, Bao W, Wang C Z, Wang Y, Qiu Z Q, Cava R J, Louie S G, Xia J and Zhang X 2017 *Nature* **546** 265
[18] Fei Z Y, Huang B, Malinowski P, Wang W B, Song T C, Sanchez J, Yao W, Xiao D, Zhu X Y, May A F, Wu W D, Cobden D H, Chu J H and Xu X D 2018 *Nat. Mater.* **17** 778
[19] Bonilla M, Kolekar S, Ma Y J, *et al.* 2018 *Nat. Nanotechnol.* **13** 289
[20] Zhao Y B, Wan Y, Huang C X, Gu P F, Zhang X M, Wu Y C, Liu M Y, Li Y, Wang K Y and Kan E J 2025 *J. Am. Chem. Soc.* **147** 31212
[21] Zhang X Q, Li P and Bian G 2025 *Rep. Prog. Phys.* **88** 086501

[22] Matsuoka H, Kajihara S, Nomoto T, Wang Y, Hirayama M, Arita R, Iwasa Y and Nakano M 2024 *Sci. Adv.* **10** 1415
[23] Kulish V V and Huang W 2017 *J. Mater. Chem. C* **5** 8734
[24] Wang W J, Sun R, Shen W, Jia Z Y, Deepak F L, Zhang Y J and Wang Z C 2023 *Nanoscale* **15** 4628
[25] Mishra P and Baruah T 2024 *J. Mater. Chem. C* **12** 5213
[26] Xie F Y, Yin Z Y, Zhou B Z and Ding Y H 2023 *Phys. Chem. Chem. Phys.* **25** 32515
[27] Liu Y Q, Liu Q X, Liu Y, Jiang X, Zhang X L and Zhao J J 2021 *Nanoscale* **13** 7714
[28] Zhang W X, Li Y, Jin H and She Y C 2019 *Phys. Chem. Chem. Phys.* **21** 17740
[29] He J J, Li X, Lyu P B and Nachtigall P 2017 *Nanoscale* **9** 2246
[30] Chen Q, Wang R Q, Huang Z C, Yuan S J, Wang H W, Ma L and Wang J L 2021 *Nanoscale* **13** 6024
[31] Wang Y, Xu W, Yang D Y, Zhang Y, Xu Y J, Cheng Z X, Mi X K, Wu Y Z, Liu Y, Hao Y and Han G Q 2023 *ACS Nano* **17** 24320
[32] Liu X F, Wang H D, Chen Z, Zhu W D, Li Z J, Hu W, Xiao H X and Zeng X C 2024 *Nano Lett.* **24** 35
[33] Miao N H, Xu B, Zhu L G, Zhou J and Sun Z M 2018 *J. Am. Chem. Soc.* **140** 2417
[34] Feng Y L, Wang Z L, Liu N and Yang Q 2023 *Nanoscale* **15** 4546
[35] Tang C, Ostrikov K, Sanvito S and Du A J 2021 *Nanoscale Horiz.* **6** 43
[36] Yuan X H, Xu M L, Huang C X, Liang Y W, Lin S Y, Hao J and Li Y W 2022 *J. Mater. Chem. C* **10** 4365
[37] Yao X J and Zhang X Y 2020 *J. Mater. Chem. C* **8** 14805
[38] Zhang Z W, Shang J Z, Jiang C Y, Rasmita A, Gao W B and Yu T 2019 *Nano Lett.* **19** 3138
[39] Son J, Son S H, Park P, Kim M, Tao Z, Oh J Y, Lee T Y, Lee S Y, Kim J Y, Zhang K X, Cho K, Kamiyama T, Lee J H, Mak K F, Shan J, Kim M Y, Park J G and Lee J 2021 *ACS Nano* **15** 16904
[40] Pancholi A, Negi P, Samanta K, Das A, Yanda P, Pandey S K and Roychowdhury S 2025 *J. Am. Chem. Soc.* **147** 35339
[41] Liu Z Y, Zhou B Z, Wang X C and Mi W B 2023 *Phys. Chem. Chem. Phys.* **25** 25146
[42] Wang X L, Guo H M, Chen H, Yan L, Xie J J, Zhang Y H, Lv J and Wu H S 2023 *Appl. Surf. Sci.* **623** 157084
[43] Ma S Q, Jiang J X, Zou L L, Lin J Q, Lu N, Zhuo Z W, Wu X J and Li Q X 2023 *Nanoscale* **15** 14912
[44] Chen Q, Ding Q Y, Wang Y T, Xu Y H and Wang J L 2020 *J. Phys. Chem. C* **124** 12075
[45] Zhao H B, Wang H G, Tan W, Ren N, Ding L H, Yu X and Wang A Z 2023 *Phys. Chem. Chem. Phys.* **25** 31050
[46] Wang B, Wu Y X, Bai Y H, Shi P Y, Zhang G B, Zhang Y G and Liu C 2023 *Nanoscale* **15** 13402
[47] Moaied M 2024 *Chin. J. Phys.* **87** 354
[48] Ma Y B, Wu Y Z, Tong J W, Deng L, Yin X, Zhou L Q, Han X L, Tian F B and Zhang X M 2023 *Nanoscale* **15** 8278
[49] Huang C X, Feng J S, Wu F, Ahmed D, Huang B, Xiang H J, Deng K M and Kan E J 2018 *J. Am. Chem. Soc.* **140** 11519
[50] Zhu H R, Shao B and Zuo X 2023 *npj Comput. Mater.* **9** 56
[51] Zhang X W, Wang B, Guo Y L, Zhang Y H, Chen Y F and Wang J L 2019 *Nanoscale Horiz.* **4** 859
[52] Han F J and Yang G C 2024 *J. Mater. Chem. C* **12** 6663
[53] Guo X P, Guo Y Q, Yin L H and He Q 2022 *Chin. Phys. B* **31** 037501
[54] Lee S Y, Hwang J Y, Park J, Nandadasa C N, Kim Y, Bang J, Lee K, Lee K H, Zhang Y W, Ma Y M, Hosono H, Lee Y H, Kim S G and Kim S W 2020 *Nat. Commun.* **11** 1526
[55] Richter J H, Ruck B J, Simpson M, *et al.* 2011 *Phys. Rev. B* **84** 235120
[56] Hewett W F H, Buckley R G, Ruck B J, Natali F and Trodahl H J 2019 *Phys. Rev. B* **99** 205131
[57] Tokmachev A M, Averyanov D V, Taldenkov A N, Parfenov O E, Karateev I A, Sokolov I S and Storozhilov V G 2019 *Mater. Horiz.* **6** 1488
[58] Li C Q and An Y K 2023 *Phys. Rev. B* **107** 115428
[59] Li S J and Lv J P 2024 *J. Appl. Phys.* **136** 063901
[60] Liu W Q, Tong J W, Deng L, Yang B, Xie G M, Qin G W, Tian F B and Zhang X M 2021 *Mater. Today Phys.* **21** 100514
[61] Wang B, Zhang X W, Zhang Y H, Yuan S J, Guo Y L, Dong S and Wang J L 2020 *Mater. Horiz.* **7** 1623
[62] Bai Y H, Wu Y X, Jia C B, Hou L P and Wang B 2023 *Appl. Phys. Lett.* **123** 012401
[63] Gao Z H, Yin Y H, Wang Y W, Cui Z C, Cao T F, Shi J Q and Fan X L 2023 *Phys. Chem. Chem. Phys.* **25** 22782
[64] Li C Q and An Y K 2023 *Nanoscale* **15** 8304
[65] Luo J, Ou K, Tang Y L, Zhang W T, Ni Y X, Wang H Y and Lan M 2023 *Eur. Phys. J. Plus* **138** 563
[66] Hu Y, Song Y L, Huang Y H, Cao S Y and Yang Y 2025 *RSC Adv.* **15** 2163
[67] Han M K, Maleski K, Shuck C E, Yang Y Z, Glazar J T, Foucher A C, Hantanasirisakul K, Sarycheva A, Frey N C, May S J, Shenoy V B, Stach E A and Gogotsi Y 2020 *J. Am. Chem. Soc.* **142** 19110
[68] Li S, He J J, Grajciar L and Nachtigall P 2021 *J. Mater. Chem. C* **9** 11132
[69] Zhang H H, Lou Y Y, Wu D N, Liao Y F and Xie J 2024 *Phys. Chem. Chem. Phys.* **26** 12681
[70] Zhang C M, Nie Y H, Sanvito S and Du A J 2019 *Nano Lett.* **19** 1366
[71] Wang Y W, Yang M H, Cui Z C, Zeng H H, Zhang X, Shi J Q, Cao T F and Fan X L 2023 *J. Mater. Sci.* **58** 268
[72] Corkan T, Vatansever E, Aklncl Ü, Gökoglu G E, AktÜrk E and Ciraci S 2020 *J. Phys. Chem. C* **124** 12816
[73] Li S S, Hou Y F, Zhou M, Zhang F W, Shao X H and Zhang P 2023 *J. Appl. Phys.* **134** 213901
[74] Shi Y T, Jia N N, Cai J T, Lyu Z H and Liu Z F 2022 *J. Phys.: Condens. Matter* **34** 475303
[75] Sun W X, Hu Y, Song Y L, Huang Y H and Cao S Y 2025 *Molecules* **30** 2100
[76] Zhang H J, Tian Y P, Jiang C, Cai J L, Jin T and Zhang L L 2025 *Phys. Rev. B* **111** 064108
[77] Zhang H J, Tian Y P, Jiang C, Kong X R and Gong W J 2025 *Phys. Chem. Chem. Phys.* **27** 3313
[78] Li S J, Hou Y F, Zhou M, Li M L, Zheng F W and Zhang P 2025 *J. Appl. Phys.* **138** 074301
[79] Li S J, Zhou M, Li M L, Zheng F W, Shao X H and Zhang P 2026 *J. Appl. Phys.* **139** 075105
[80] Kresse G and Furthmüller J 1996 *Phys. Rev. B* **54** 11169
[81] Blöchl P E 1994 *Phys. Rev. B* **50** 17953
[82] Kresse G and Joubert D 1999 *Phys. Rev. B* **59** 1758
[83] Perdew J P, Burke K and Ernzerhof M 1996 *Phys. Rev. Lett.* **77** 3865
[84] Heyd J, Scuseria G E and Ernzerhof M 2003 *J. Chem. Phys.* **118** 8207
[85] Monkhorst H J and Pack J D 1976 *Phys. Rev. B* **13** 5188
[86] Martyna G J, Klein M L and Tuckerman M 1992 *J. Chem. Phys.* **97** 2635
[87] Parlinski K, Li Z and Kawazoe Y 1997 *Phys. Rev. Lett.* **78** 4063
[88] Carreras A, Togo A and Tanaka I 2017 *Comput. Phys. Commun.* **221** 221
[89] Maintz S, Deringer V L, Tchougreeff A L and Dronskowski R 2016 *J. Comput. Chem.* **37** 1030
[90] Grimme S, Ehrlich S and Goerigk L 2011 *J. Comput. Chem.* **32** 1456
[91] Haynes W M 2016 *CRC Handbook of Chemistry and Physics* (New York: CRC Press) p. 920
[92] Born M, Huang K and Lax M 1955 *Am. J. Phys.* **23** 474
[93] Liu J Y, Sun Q, Kawazoe Y and Jena P 2016 *Phys. Chem. Chem. Phys.* **18** 8777
[94] Kittel C and Kroemer H 1980 *Thermal Physics* (Norwalk: W. H. Freeman) p. 357
[95] Miessler G L and Tarr D A 1999 *Inorganic Chemistry* (New York: Prentice-hall) p. 358
[96] Stöhr J and Siegmann H C 2006 *Magnetism: From Fundamentals to Nanoscale dynamics.* (Berlin: Springer-Verlag) p. 274
[97] Fang Y M, Wu S Q, Zhu Z Z and Guo G Y 2018 *Phys. Rev. B* **98** 125416
[98] Hu Y, Gong Y H, Zeng H H, Wang J H and Fan X L 2020 *Nanoscale* **12** 11627
[99] Xiang H J, Lee C H, Koo H J, Gong X G and Whangbo M H 2013 *Dalton Trans.* **42** 823
[100] Dong L, Lou J and Shenoy V B 2017 *ACS Nano* **11** 8242
[101] Tan J, Wang Y H, Wang Z T, He X J, Liu Y L, Wang B, Katsnelson M I and Yuan S J 2019 *Nano Energy* **65** 104058
[102] Hu L and Huang X 2017 *RSC Adv.* **7** 55034
[103] Guo S D, Guo X S, Zhu Y T and Ang Y S 2022 *Appl. Phys. Lett.* **121** 062403
[104] Ji S L, Wu H, Zhou S, Niu W, Wei L J, Li X A, Li F and Pu Y 2020 *Chin. Phys. Lett.* **37** 087505